

Ultrafast charge carrier separation in Potassium-intercalated endohedral metallofullerene $\text{Sc}_3\text{N@C}_{80}$ thin films

Sebastian Emmerich,^{1,*} Sebastian Hedwig,¹ Mirko Cinchetti,² Benjamin Stadtmüller,¹ and Martin Aeschlimann¹

¹*University of Kaiserslautern and Research Center OPTIMAS,
Erwin-Schrödinger-Straße 46, 67663 Kaiserslautern, Germany*

²*Experimentelle Physik VI, Technische Universität Dortmund, 44221 Dortmund, Germany*

Molecular materials have emerged as highly tunable materials for photovoltaic and light-harvesting applications. The most severe challenge of this class of materials is the trapping of charge carriers in bound electron-hole pairs, which severely limits the free charge carrier generation. Here, we demonstrate a significant modification of the exciton dynamics of thin films of endohedral metallofullerene complexes upon alkali metal intercalation. For the exemplary case of $\text{Sc}_3\text{N@C}_{80}$ thin films, we show that potassium intercalation results in an additional relaxation channel for the optically excited charge-transfer excitons that prevents the trapping of excitons in a long-lived Frenkel exciton-like state. Instead, K intercalation leads to an ultrafast exciton dissociation coinciding most likely with the generation of free charge carriers. In this way, we propose alkali metal doping of molecular films as a novel approach to enhance the light to-charge carrier conversion efficiency in photovoltaic materials.

1. INTRODUCTION

Designing and functionalizing materials for dedicated areas of application is one of the biggest promises of materials science, aiming to advance the performance of next generation technology. One of the most important quests in this field is to uncover and optimize materials for light harvesting and photovoltaic applications to create renewable sources¹, which are able to convert solar energy into charge and spin carriers with utmost energy efficiency.

From the manifold of photovoltaic materials^{2–5}, one of the most promising candidates to supplement or even replace today's compounds are molecular materials. Besides low cost production and sustainability, the most intriguing property of these materials is their chemical tunability. This allows one to actively control the two most crucial material properties for the device efficiency on a single molecular scale, namely the spectral light absorption efficiency and the charge carrier transport⁶. For instance, they can be manipulated or controlled by the choice of the molecular core and the molecular ligands^{7–10}.

A very special and extremely tunable case in this context are fullerenes such as the buckminsterfullerene C_{60} . Their properties can be tailored either by changing the number of atoms of the carbon cage itself or by incorporating atoms or small clusters of atoms into the carbon cage, forming so called endohedral metallofullerenes (EMFs)^{11,12}. The latter offers the particular opportunity to embed spin-carrying atoms into the carbon cage to form single molecular magnets, or to manipulate the charge transport properties^{7,13} and excited state dynamics¹⁴ of EMF films by the appropriate choice of the metallic cluster inside the carbon cage.

In this Letter, we explore the ultrafast dynamics of functionalized EMF materials after optical excitation

with fs-light pulses. The excited state dynamics provide a direct view onto the microscopic mechanism mediating or limiting the light-to-charge conversion efficiency in molecular materials. In contrast to inorganic metals or semiconductors, the optical excitation of molecular materials with visible light does not result in the formation of free carriers, but in bound electron-hole pairs, so called excitons, with binding energies up to several hundred meV¹⁵. These excitons can exhibit different charge distributions and different degrees of spatial delocalization, which are typically described in the limit of charge-transfer (CT) and Frenkel excitons and can have long depopulation (decay) times up to several hundreds of microseconds. The long depopulation times of the energetically lowest excitonic level as well as its large exciton binding energy severely limit the optically induced free carrier generation in molecular materials, a challenge that must be tackled to improve the performance of molecular-based photovoltaic applications.

Therefore, we focus on the tunability of the exciton dynamics of EMF materials by potassium (K) intercalation. As exemplary case, we have selected the tri-metallic nitride fullerene $\text{Sc}_3\text{N@C}_{80}$. It consists of a very robust C_{80} carbon cage, which encapsulates three scandium (Sc) atoms coordinated to a central nitrogen (N) atom. This member of the EMF family is particularly interesting since the lowest unoccupied molecular orbital (LUMO) is not located at the carbon cage, but predominantly at the Sc_3N core¹⁶. This enables us not only to study the exciton dynamics at the carbon cage, but also to gain insights into potential cluster-cage charge transfer phenomena on ultrafast timescales.

In the following, we will show that K intercalation has a significant influence on the exciton dynamics of thin films of the prototypical endohedral metallofullerene $\text{Sc}_3\text{N@C}_{80}$. Using time-resolved photoemission with fs-XUV radiation, we find that the exciton dynamics of the pristine (undoped) molecular film after optical exciton with visible light are dominated by an exciton decay cascade starting from the thermalization of optically excited

*Electronic address: emmerich@physik.uni-kl.de

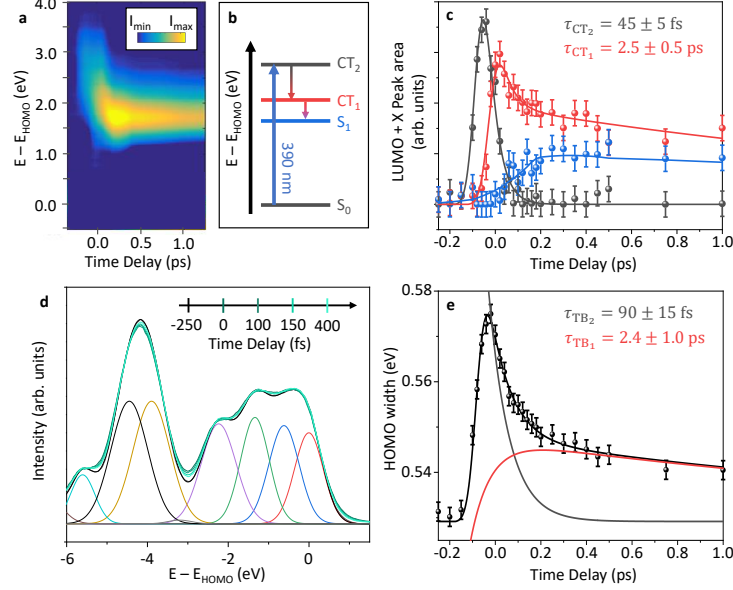


FIG. 1: *Electron dynamics in a pristine $\text{Sc}_3\text{N@C}_{80}$ multilayer film.* **a** Excitons are created with a fs 3.2 eV laser pulse and subsequently decay into energetically lower excitonic states. **b** The energy level diagram shows the energetic position of the excitons CT_2 , CT_1 and S_1 . **c** Population dynamics of the three excitonic levels shown in panel b. **d** Valence band structure of the studied $\text{Sc}_3\text{N@C}_{80}$ film for different pump-probe time delays (shown in green colors). The colored peaks show the contributions of the fitting model for the quasi-static ($\Delta t = -250$ fs) spectrum (for other time steps, refer to Fig. S3). **e** Transient change of the linewidth for the HOMO state (dots), fitted with a double exponential decay function convoluted with the pump-probe cross correlation curve (solid line).

CT excitons to a trapping of the excited states in a long-lived Frenkel exciton. Upon K intercalation, the decay cascade ends after the thermalization of the CT excitons which dissolve on sub-500 fs timescales. We propose that this modification is caused by the dissociation of CT excitons due to the interaction with the K-atoms resulting in the generation of free charge carriers in homo-molecular materials on ultrafast timescales.

2. RESULTS AND DISCUSSION

2.1. Ultrafast exciton dynamics of pristine $\text{Sc}_3\text{N@C}_{80}$ thin films

We start our discussion with the ultrafast dynamics of the pristine $\text{Sc}_3\text{N@C}_{80}$ thin film ($\Theta_{\text{Sc}_3\text{N@C}_{80}} \approx 10$ ML). The exciton dynamics were investigated in real-time using time-resolved photoelectron spectroscopy with fs-XUV radiation (experimental details can be found in the supplementary information). Crucially, the photon energy allows us to simultaneously monitor the excited state dynamics as well as the transient changes in the occupied valence levels of the entire molecular film. The latter can reveal characteristic transient spectral changes upon optical excitation, such as a transient linewidth broadening of all molecular valence states, which was recently identified as the transient spectroscopic signatures

of CT excitons in molecular films¹⁷.

The exciton dynamics of the $\text{Sc}_3\text{N@C}_{80}$ film are shown as a two-dimensional plot of the time-dependent photoemission intensity in Fig. 1a. After optical excitation with 3.2 eV photons, we observe the instantaneous accumulation of spectral density 2.8 eV above the highest occupied molecular orbital (HOMO) of the $\text{Sc}_3\text{N@C}_{80}$ molecule. This photoemission signal is identified as the CT_2 level, which is resonantly excited from the HOMO level (S_0 in Fig. 1b) of the molecular film. This transient population decays into the CT_1 level at 2.1 eV above E_{HOMO} before becoming trapped in the excited state S_1 at $E - E_{\text{HOMO}} = 1.7$ eV with a depopulation time of $\tau_{\text{S}_1} \gg 1$ ps. This decay cascade is summarized in the energy diagram in Fig. 1b.

To quantify the exciton dynamics, we employed a fitting model with three Gaussian curves to model the time-dependent spectral density of the three states CT_2 , CT_1 and S_1 . During our fitting routine, we constrained the excited state energy and the linewidth (full width at half maximum, FWHM) of each excited state to a fixed value. The only free fitting parameter is the peak intensity (area) of each Gaussian curve, which reflects the population of each excitonic level (more details see supporting information).

The measured population dynamics of each excitonic state is shown in Fig. 1c as colored dots. The solid lines of identical color represent the fitting model to determine

the depopulation (decay) time of each excitonic state. The CT_2 exciton is formed instantaneously after the optical exciton (within our experimental uncertainty) and directly decays into the lower lying CT_1 exciton within $\tau_{CT_2} = 45 \pm 5$ fs (black curve). The decay dynamics of CT_1 can only be described by a double-exponential decay (see red curve in figure 1c) with two significantly different depopulation times of $\tau_{CT_1,1} = 50 \pm 5$ fs and $\tau_{CT_1,2} = 2.5 \pm 1.0$ ps. Subsequently, the population of the S_1 exciton increases within the first 200 fs before staying almost constant for all times investigated in our experiment. This points to an excitonic lifetime of the S_1 level of $\tau_{S_1} \gg 10$ ps.

The double-exponential decay trace of CT_1 suggests the existence of at least two excitonic states in this excited state range which could not be separated in our data. In fact, the spectral shape of the excited states changes continuously during the transition from the CT_2 to the CT_1 exciton. However, no reliable fitting results were obtained when allowing a continuous change of the spectral line shape of the CT_2 exciton. Therefore, we had to limit our fitting model to three excitonic states CT_2 , CT_1 and S_1 at fixed excited state energies.

The spatial charge distribution of the three excitonic states can be revealed by analyzing the occupied valence states' dynamics. Figure 1d shows the general trend of the optically induced band structure dynamics of the occupied molecular levels by displaying selected EDCs for characteristic time steps of the previously observed exciton dynamics in the excited states. First, before optical excitation ($\Delta t = -250$ fs), the quasi-static spectral line-shape of the HOMO level as well as the lower lying molecular orbitals (HOMO-X) reflect perfectly the spectroscopic findings of previous studies of $Sc_3N@C_{80}$ multilayer films on different surfaces^{18,19}. Upon optical excitation and creation of excitons, the linewidth of all molecular features increases before transforming back to its original state. The relaxation dynamics are significantly slower than the excitation and occur only within several hundreds of fs. This transient broadening of all molecular valence orbitals reflects the many-body response of the molecular material to the optically induced excitons, caused by electronic correlations and dielectric screening. Even more importantly, the transient broadening was recently identified as the spectroscopic signature of CT excitons in the molecular material¹⁷ and hence clearly hints at an at least partial CT character of the optically excited excitons in the $Sc_3N@C_{80}$ film.

The transient changes of the spectral linewidth were quantified by applying a dedicated fitting routine (see SI for a detailed description of the valence orbital fitting routine). The extracted transient evolution of the linewidth of the HOMO level is shown in Fig. 1e. We find an instant rise of the transient linewidth after optical excitation within our fs temporal resolution²⁰ followed by a double-exponential decay with two significantly different time constants. These time constants are $\tau_{TB_2} = 90 \pm 15$ fs and $\tau_{TB_1} = 2.5 \pm 0.5$ ps. These time constants match almost perfectly the depopulation times

of the CT_2 and the CT_1 excitons, but not the one of the S_1 exciton. Therefore, only the CT_2 and CT_1 excitons reveal partial CT character.

Together, our findings for exciton population dynamics (excited states) and the transient charge character of the excitons (valence states) provides a clear picture of the exciton dynamics in the pristine $Sc_3N@C_{80}$ film. Optical exciton with 3.2 eV photons results in the instantaneous formation of hot excitons with at least partial CT character (referred to as CT_2). These CT_2 excitons thermalize within 100 fs and transform continuously into the CT_1 excitons with lower excited state energy. In a second step, the thermalized CT_1 excitons decay further into the S_1 exciton with dominant Frenkel exciton-like character where they become trapped for at least 10 ps. Interestingly, the energy of the S_1 exciton ($E - E_{HOMO} = 1.7$ eV) is still significantly larger than the energy of the LUMO-derived molecular state inside the carbon cage^{18,19}. This suggests that the exciton dynamics of all three excitonic states CT_2 , CT_1 and S_1 only involve excited states that are located at the carbon cage, but not at the Sc_3N core. It is hence very similar to the exciton dynamics of the prototypical fullerene C_{60} ¹⁷.

2.2. Exciton dynamics of a K-intercalated $K_1(Sc_3N@C_{80})$ thin film

We now turn to the modification of the exciton dynamics of the $Sc_3N@C_{80}$ film after K intercalation and start with a K concentration with one K-atom per $Sc_3N@C_{80}$ molecule ($x = 1$).

First of all, K intercalation of the pristine $Sc_3N@C_{80}$ thin film results in a spectral broadening of the valence band structure coinciding with a work function decrease of $\Delta\Phi = 0.5 \pm 0.05$ eV¹⁹. This spectral broadening has its origin in the lifting of the degeneracy of the π -orbitals located at the C_{80} cage, which is caused by the reduced cage symmetry of the doped fullerene cage²¹. The most important change, however, is the population of the LUMO-derived state located at the Sc_3N core. It becomes occupied by the CT from the K-dopant atom to the $Sc_3N@C_{80}$ and leads to a new spectroscopic feature in the molecular valence band structure located 0.85 eV above E_{HOMO} ^{16,19}. It is marked by a black Gaussian curve in the spectra in Fig. 2d.

Besides these spectral changes, K intercalation has a strong effect on the optically induced exciton dynamics of the $K_1(Sc_3N@C_{80})$ thin film which is summarized in Fig. 2. The measured excited state dynamics are shown in Fig. 2a, the corresponding energy level diagram in Fig. 2b. Optical excitation results in the instantaneous formation of hot excitons 2.8 eV above E_{HOMO} (CT_2). Subsequently, these hot CT_2 excitons thermalize and continuously decay into the excitonic level CT_1 at lower energies. The exciton population is trapped in the CT_1 exciton for a few hundreds of fs before vanishing from the excited states. In particular, we do not observe any indication for a long-lived trapping of excitons in the S_1

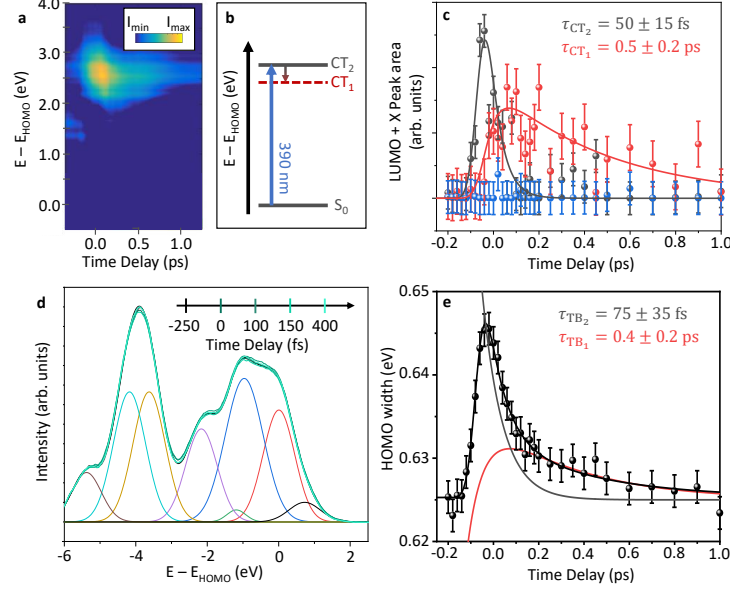


FIG. 2: *Electron dynamics in a K-intercalated $K_1(\text{Sc}_3\text{N}@\text{C}_{80})$ multilayer film.* **a** Excitons are created with a fs 3.2 eV laser pulse and subsequently decay into energetically lower excitonic states. **b** The energy level diagram shows the energetic position of the excitons CT_2 and CT_1 . **c** Population dynamics of the excitonic levels shown in panel b. Besides CT_2 and CT_1 , the excitonic state S_1 , populated during the decay cascade of the pristine $\text{Sc}_3\text{N}@\text{C}_{80}$ film (see fig. 1), has been included in the fitting routine (blue dots), but is not populated for the K-intercalated case (compare Fig. S2). **d** Valence band structure of the studied K-intercalated $\text{Sc}_3\text{N}@\text{C}_{80}$ film for different pump-probe time delays (shown in green colors). The colored peaks show the contributions of the fitting model for the quasi-static spectrum at $\Delta t = -250$ fs (for other time steps, refer to Fig. S4). **e** Transient change of the linewidth for the HOMO state (dots), fitted with a double exponential decay function convoluted with the pump-probe cross correlation curve (solid line).

level as discussed beforehand for the pristine $\text{Sc}_3\text{N}@\text{C}_{80}$ films.

The time scales of the exciton decay cascade can be determined from the transient population of the CT_2 and the CT_1 state shown in Fig. 2c. These values were extracted from the time-resolved photoemission data by using Gaussian curves at fixed excited state energies as discussed above. The best fitting result was obtained for a slightly larger excited state energy of Gaussian peak modelling the thermalized CT_1 excitons. Interestingly, no population could be detected for the energy position of the S_1 exciton (blue data points). Using exponential decay functions, we observe depopulation times of $\tau_{\text{CT}_2, \text{K}} = 50 \pm 15$ fs and $\tau_{\text{CT}_1, \text{K}} = 0.5 \pm 0.2$ ps for the CT_2 and CT_1 excitons. The depopulation time for the CT_1 state is hence almost one order of magnitude smaller after K intercalation than in the pristine $\text{Sc}_3\text{N}@\text{C}_{80}$ film. These time scales can be directly compared to each other as the K intercalation study was conducted on the same sample as the study of the exciton dynamics of the pristine $\text{Sc}_3\text{N}@\text{C}_{80}$ film. This suggests a new and significantly faster decay (or energy dissipation) mechanism for the thermalized CT_1 excitons due to the presence of K impurities.

These changes are also reflected in the transient linewidth broadening ΔFWHM of the valence states. EDCs at selected time delays are shown in Fig. 2d, the

extracted transient linewidth broadening of the HOMO is illustrated in Fig. 2e. Similar to the pristine $\text{Sc}_3\text{N}@\text{C}_{80}$ film, there is an immediate broadening of the HOMO upon the excitation followed by a double-exponential decay back to the initial spectral linewidth. The decay times extracted from the double-exponential decay fit are $\tau_{\text{TB}_2, \text{K}} = 75 \pm 35$ fs and $\tau_{\text{TB}_1, \text{K}} = 0.4 \pm 0.2$ ps, respectively. Both decay times match the depopulation times of the CT_2 and CT_1 excitons in the excited states, demonstrating that both types of excitons still reveal dominant CT character, even after K intercalation.

Hence, K intercalation results in a significantly faster decay of the thermalized charge-transfer excitons CT_1 compared to the CT_1 excitons of the pristine $\text{Sc}_3\text{N}@\text{C}_{80}$ thin films. Crucially, these CT_1 excitons do not decay into lower lying excitonic levels, such as the S_1 exciton for the pristine film, but disappear completely from the excited state spectra. These observations could either be attributed to a direct recombination of the electron and hole of the CT_1 exciton, i.e., to a direct decay of the CT_1 exciton into the ground state, or to an efficient exciton dissociation and the generation of free carriers. In the following, we tackle this question by studying the correlation between the exciton dynamics of K-intercalated $\text{Sc}_3\text{N}@\text{C}_{80}$ thin films for various K concentrations.

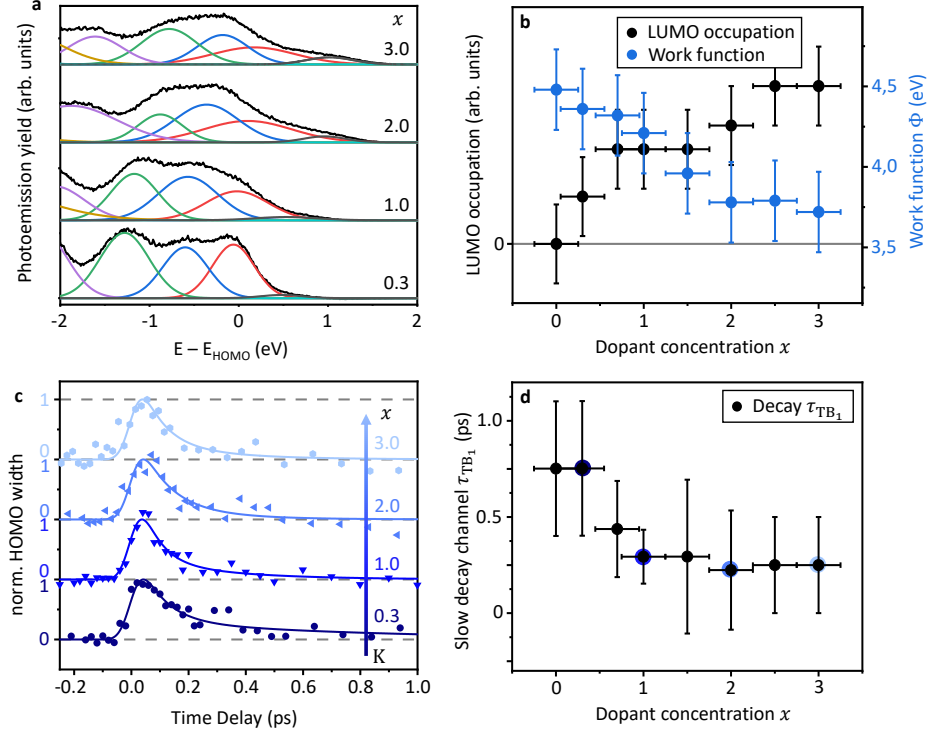


FIG. 3: *K* concentration-dependent intercalation study of a $K_x(\text{Sc}_3\text{N}@C_{80})$ multilayer film. **a** Valence band photoemission spectra of $K_x(\text{Sc}_3\text{N}@C_{80})$ for selected intercalation steps (see supplementary figure S5b for all datasets). The K concentration x has been estimated by comparison of valence band photoemission spectra with literature¹⁹ (compare figure S5a). The line-shape of the Gaussian curves show the contributions to the valence band photoemission spectra of $K_x(\text{Sc}_3\text{N}@C_{80})$. **b** Increasing LUMO occupation (black dots; left vertical scale) and decreasing work function (blue dots; right vertical scale) extracted from the fit of the valence orbital photoemission spectra in **a** as a function of dopant concentration x . **c** Normalized transient HOMO linewidth for selected intercalation steps (shifted vertically for better comparability). All data sets are shown in supplementary figure S5c. **d** Extracted decay time τ_{TB_1} for different dopant concentrations x . The decay time decreases for K concentrations $x > 0.3$. Colored data points are extracted from the respective graph in **c**. All data sets used for extraction of the shown data are shown in supplementary figure S5c.

2.3. K concentration-dependent exciton dynamics of $K_x(\text{Sc}_3\text{N}@C_{80})$ thin films

The K concentration-dependent exciton dynamics of the $\text{Sc}_3\text{N}@C_{80}$ thin film are shown in Fig. 3. The K concentration of each intercalation step was identified by the characteristic line-shape of the (static) valence band structure¹⁹ which is shown in Fig. 3a for selected K concentrations x . The continuous broadening of the valence band structure with increasing K concentration can be attributed to a K-induced structural distortion of the C_{80} cage coinciding with a change in the cage symmetry and a lifting of the energy degeneracy of the molecular valence orbitals^{16,19,21}. In addition, increasing the K concentration results in a gradual population of the LUMO-derived state at the Sc_3N core due to a charge transfer from the K atoms into the molecule. The amount of charge transfer can be estimated by the spectral weight of the corresponding LUMO-derived feature in the valence band spectra which emerges at 0.85 eV above E_{HOMO} (black Gaussian curve in Fig. 2d and Fig. 3a). It is shown in Fig. 3b as black data points together with the K

concentration-dependent decrease of the work function.

For each intercalation step x , the excited states and the transient evolution of the valence states were studied by time-resolved photoemission. Here, we focus our discussion on the K-induced modifications of the population dynamics of the excitons with dominant CT character, which dominate the first steps of the exciton thermalization and decay process in fullerene materials. Their dynamics are fully reflected in the transient linewidth broadening of the molecular valence bands which is shown for the exemplary case of the HOMO level in Fig. 3c for selected K concentrations x . The transient linewidth of the HOMO has been normalized to its linewidth before optical excitation for better comparability of the K-dependent transient linewidth traces. All transient linewidth traces were analyzed by the double-exponential decay model presented earlier and resulted in K concentration-dependent decay times $\tau_{\text{TB}_2}(x)$ and $\tau_{\text{TB}_1}(x)$. Within our experimental uncertainty, the fast decay time $\tau_{\text{TB}_2}(x)$, connected to the initial optical excitation, stays constant for all K concentrations, which suggests that the thermalization dynamics of the opti-

cally excited, hot CT_2 excitons do not depend on the amount and density of the K atoms within the $\text{Sc}_3\text{N@C}_{80}$ films.

In contrast to the dynamics of the hot CT_2 excitons, we find two characteristic intercalation regimes for the K-dependent dynamics of the more thermalized CT_1 excitons which are shown in Fig. 3d. In the first regime between $0.3 < x < 1$, the depopulation times $\tau_{\text{TB}_1}(x) = \tau_{\text{CT}_1}(x)$ of CT_1 change quantitatively and decrease from 0.75 ± 0.25 ps to 0.25 ± 0.2 ps, i.e., the average speed of the exciton decay process increases with increasing K concentration. In parallel, we observe a reduction of the spectral yield of the S_1 exciton, which completely vanishes for K concentrations $x \geq 1$. In this regime, we observe a saturation of $\tau_{\text{TB}_1}(x \geq 1)$ at 0.25 ± 0.2 ps and the disappearance of any signature of the S_1 excitonic level in the excited states. Hence, there is a characteristic and qualitative modification of the exciton dynamics of the $\text{K}_x(\text{Sc}_3\text{N@C}_{80})$ films above the critical K concentration of $x = 1$. Therefore, the exciton dynamics of the $\text{K}_1(\text{Sc}_3\text{N@C}_{80})$ film discussed above are representative for all K concentrations in this regime ($x \geq 1$).

Interestingly, the transition of the exciton dynamics occur for a K concentration with one K atom per $\text{Sc}_3\text{N@C}_{80}$ and not at $x = 2$, where the lowest LUMO state, located at the core, would be completely occupied (see Fig. 3d). This suggests that the population of the LUMO level is not the decisive factor in the qualitative transition of the exciton dynamics since population-induced blocking of final states for the exciton relaxation process can only occur efficiently for fully occupied molecular orbitals. Instead, we propose that the direct decay or dissociation of the CT_1 is most likely triggered by the spatial vicinity of the CT exciton and the K atom.

3. CONCLUSION

Our experimental findings have demonstrated the decisive influence of K intercalation on the exciton decay processes of endohedral metallofullerenes. The exciton dynamics of the pristine $\text{Sc}_3\text{N@C}_{80}$ thin film reveal the typical exciton dynamics of fullerene thin films^{17,22–24}, i.e., the wave functions of the excitonic level are mainly localized on the carbon cage. First, optical excitation with visible light results in the formation of hot excitons with CT character (CT_2). These hot CT_2 excitons relax within sub-100 fs into thermalized CT excitons (CT_1) with significantly longer depopulation times in the order of 1 ps. Finally, the excitons relax into a Frenkel-like excitonic level S_1 in which they become trapped for several ps.

After K intercalation, the exciton dynamics of the molecular material are strongly modified above a characteristic step, corresponding to a distinct K concentration regime. For moderate doping concentrations with less than one K atom per $\text{Sc}_3\text{N@C}_{80}$, we observe a continuous reduction of the depopulation times of the CT_1 and a decreasing maximal population of the S_1 exciton which

increasing K concentration. For larger K concentrations with at least one K atom per $\text{Sc}_3\text{N@C}_{80}$ molecule, the CT_1 excitons no longer decay into the energetically lower S_1 state, but directly dissolve or dissociate with a constant depopulation time below 0.5 ps.

Most importantly, the characteristic transition between these two exciton decay processes occurs below one K atom per $\text{Sc}_3\text{N@C}_{80}$ molecule. This suggests that either the direct spatial vicinity between the CT excitons and the K dopants or a minimum charge transfer between the K dopants and the $\text{Sc}_3\text{N@C}_{80}$ molecules is required for the modification of the excitation dynamics.

Charge transfer into the $\text{Sc}_3\text{N@C}_{80}$ molecule results in an occupation of the $3d$ orbitals of the Sc atoms in the metal core coinciding with a reducing of the wave function overlap between the Sc_3N cluster and the C_{80} cage. This can lead to a change of the cage symmetry of the pristine $\text{Sc}_3\text{N@C}_{80}$ ^{16,19} and to lattice distortions of the molecular films²¹ upon K intercalation. This could influence the excited state decay channels for carbide-based clusterfullerenes¹⁴. However, these modifications of the structural and electronic properties of the molecules still evolve, even for K concentrations larger than one K atom per $\text{Sc}_3\text{N@C}_{80}$ molecule, as is clearly visible in our photoluminescence data in Fig. 3. This is shown, for instance, by the continuous modifications of the molecular valence band structure for K concentrations $x \geq 1$.

Therefore, our findings indicate that the interaction between CT excitons and K-dopant atoms are responsible for the qualitative transition in the exciton decay dynamics. The charge-transfer process between the K atom and the $\text{Sc}_3\text{N@C}_{80}$ molecule leads to an (at least partial) ionic character of the K-dopants in the molecular film. As a result, the dynamics of the CT excitons in the vicinity of a K ion are severely altered by the interaction of the microscopic charge distribution of the CT excitons and the Coulomb potential of the K ions. This additional interaction opens a new relaxation pathway either towards the recombination of the electron and hole of the exciton or towards exciton dissociation and the generation of free charge carriers. An enhanced exciton decay via recombination is more likely in molecular materials with enhanced structural or charge order which, for instance, occurs by reducing the thermal motion of the molecules using e.g. temperature^{25,26}. This is clearly different in our case, where K intercalation results in the lattice distortions of the $\text{Sc}_3\text{N@C}_{80}$ molecule and the increase of K defect sites that break the translation symmetry of the molecular layer. Therefore, we propose that K interaction significantly enhances the speed and efficiency of the free charge carrier generation via exciton dissociation. Possibly, the ionic K dopants are able to capture the electron of the excitation via Coulomb attraction resulting in the generation of free holes in the $\text{Sc}_3\text{N@C}_{80}$ film.

Finally, we would like to point out that our model can also explain the independence of the depopulation time of the CT_1 exciton on K intercalation for low intercalation concentrations. For low K concentrations, the

probability to create CT excitons in direct vicinity of a K atom is rather low due to the random distribution of the K dopants in the molecular film and the stochastic process of the optical excitation. Hence, only a small number of CT excitons can dissociate via the ultrafast K-mediated relaxation channel while the other CT excitons decay with the intrinsic depopulation time of the pristine films before becoming trapped in the S_1 state. Our photoemission experiment spatially averages over all these processes and the recorded signal is composed of both decay processes according to their relative contributions. With increasing K concentration, the relative contribution of the direct exciton dissociation process increases and the average depopulation time constant of CT_1 decreases until it saturates at $x = 1$. At this point, all CT excitons decay via the much faster relaxation channel mediated by the K intercalation-induced charge defects.

In conclusion, our investigation of the exciton dynamics in K-intercalated endohedral metallofullerenes has demonstrated the decisive role of alkali metal intercalation on the ultrafast exciton dynamics of molecular materials. We uncovered a K-induced ultrafast relaxation mechanism that prevents the trapping of excitons in

long-lived excitonic states and results, most likely, in the generation of free charge carriers on ultrafast, sub-500 fs timescales. We therefore propose alkali metal doping of molecular films as a novel approach to enhance the light-to-charge carrier conversion efficiency in photovoltaic materials that could potentially pave the way towards the next generation of molecular-based light-harvesting applications with superior performance.

Acknowledgments

The research leading to these results was financially supported by the Deutsche Forschungsgemeinschaft (DFG, SFB/TRR 88 Cooperative Effects in Homo- and Heterometallic Complexes (3MET) Project C9). Furthermore, B.S. and S.E. acknowledge financial support from the Graduate School of Excellence Mainz (Excellence initiative DFG/GSC 266). This work is supported by the European Research Council (Grant 725767-hyControl).

-
- ¹ G. K. Singh, *Energy* **53**, 1 (2013).
 - ² K. Yoshikawa, H. Kawasaki, W. Yoshida, T. Irie, and E. Al, *Nat. Energy* **2** (2017).
 - ³ W. S. Yang, J. H. Noh, N. J. Jeon, Y. C. Kim, S. Ryu, J. Seo, and S. I. Seok, *Science* **348**, 1234 (2015).
 - ⁴ L. Meng, Y. Zhang, X. Wan, C. Li, X. Zhang, Y. Wang, X. Ke, Z. Xiao, L. Ding, R. Xia, et al., *Science* **361**, 1094 (2018).
 - ⁵ J. Albero, P. Atienzar, A. Corma, and H. Garcia, *Chem. Rec.* **15**, 803 (2015).
 - ⁶ W. Shockley and H. J. Queisser, *J. Appl. Phys.* **32**, 510 (1961).
 - ⁷ R. B. Ross, C. M. Cardona, F. B. Swain, D. M. Guldi, S. G. Sankaranarayanan, E. Van Keuren, B. C. Holloway, and M. Drees, *Adv. Funct. Mater.* **19**, 2332 (2009).
 - ⁸ M. Schwarze, W. Tress, B. Beyer, F. Gao, R. Scholz, C. Poelking, K. Ortstein, A. A. Günther, D. Kasemann, D. Andrienko, et al., *Science* **352**, 1446 (2016).
 - ⁹ J. R. Pinzón, M. E. Plonska-Brzezinska, C. M. Cardona, A. J. Athans, S. S. Gayathri, D. M. Guldi, M. Á. Herranz, N. Martín, T. Torres, and L. Echegoyen, *Angew. Chemie - Int. Ed.* **47**, 4173 (2008).
 - ¹⁰ O. Ostroverkhova, *Chem. Rev.* **116**, 13279 (2016).
 - ¹¹ S. Stevenson, G. Rice, T. Glass, K. Harlch, F. Cromer, M. R. Jordan, J. Craft, E. Hadju, R. Bible, M. M. Olmstead, et al., *Nature* **401**, 55 (1999).
 - ¹² A. Popov, S. Yang, and L. Dunsch, *Chem. Rev.* **113**, 5989 (2013).
 - ¹³ S. Sato, S. Seki, G. Luo, M. Suzuki, J. Lu, S. Nagase, and T. Akasaka, *J. Am. Chem. Soc.* **134**, 11681 (2012).
 - ¹⁴ B. Wu, J. Hu, P. Cui, L. Jiang, Z. Chen, Q. Zhang, C. Wang, and Y. Luo, *J. Am. Chem. Soc.* **137**, 8769 (2015).
 - ¹⁵ C. J. Bardeen, *Annu. Rev. Phys. Chem.* **65**, 127 (2014).
 - ¹⁶ A. A. Popov and L. Dunsch, *J. Am. Chem. Soc.* **130**, 17726 (2008).
 - ¹⁷ B. Stadtmüller, S. Emmerich, D. Jungkenn, N. Haag, M. Rollinger, S. Eich, M. Maniraj, M. Aeschlimann, M. Cinchetti, and S. Mathias, *Nat. Commun.* **10**, 1 (2019).
 - ¹⁸ J. Seidel, L. L. Kelly, M. Franke, G. Van Straaten, C. Kumpf, M. Cinchetti, M. Aeschlimann, and B. Stadtmüller, *Phys. Rev. B* **98**, 1 (2018).
 - ¹⁹ L. Alvarez, T. Pichler, T. Pichler, P. Georgi, T. Schwieger, H. Peisert, L. Dunsch, Z. Hu, M. Knupfer, J. Fink, et al., *Phys. Rev. B* **66**, 351071 (2002).
 - ²⁰ S. Eich, A. Stange, A. Carr, J. Urbancic, T. Popmitchew, M. Wiesenmayer, K. Jansen, A. Ruffing, S. Jakobs, T. Rohwer, et al., *J. Electron Spectros.* **195**, 231 (2014).
 - ²¹ K. Harigaya, *Phys. Rev. B* **45**, 13676 (1992).
 - ²² R. Jacquemin, S. Kraus, and W. Eberhardt, *Solid State Commun.* **105**, 449 (1998).
 - ²³ A. C. Rosenfeldt, B. Göhler, and H. Zacharias, *J. Chem. Phys.* **133** (2010).
 - ²⁴ M. Causa, I. Ramirez, J. F. Martinez Hardigree, M. Riede, and N. Banerji, *J. Phys. Chem. Lett.* **9**, 1885 (2018).
 - ²⁵ M. S. Dresselhaus, G. Dresselhaus, A. M. Rao, and P. C. Eklund, *Synth. Met.* **78**, 313 (1996).
 - ²⁶ A.-M. Janner, R. Eder, B. Koopmans, H. T. Jonkman, and G. A. Sawatzky, *Phys. Rev. B* **52**, 158 (1995).

Ultrafast charge carrier separation in Potassium-intercalated endohedral metallofullerene $\text{Sc}_3\text{N@C}_{80}$ thin films (Supplementary Information)

Sebastian Emmerich,¹ Sebastian Hedwig,¹ Mirko Cinchetti,² Benjamin Stadtmüller,¹ and Martin Aeschlimann¹

¹*University of Kaiserslautern and Research Center OPTIMAS,
Erwin-Schrödinger-Straße 46, 67663 Kaiserslautern, Germany*

²*Experimentelle Physik VI, Technische Universität Dortmund, 44221 Dortmund, Germany*

Contents

1. Supplementary Figures	2
2. Supplementary Methods	7
2.1. Experimental Setup	7
2.2. Details on the spectral analysis of excited states	7
2.3. Details on the analysis of the population decay of the excited states	8
2.4. Details on the analysis of the transient width dynamics of the occupied valence band states	8
References	9

1. SUPPLEMENTARY FIGURES

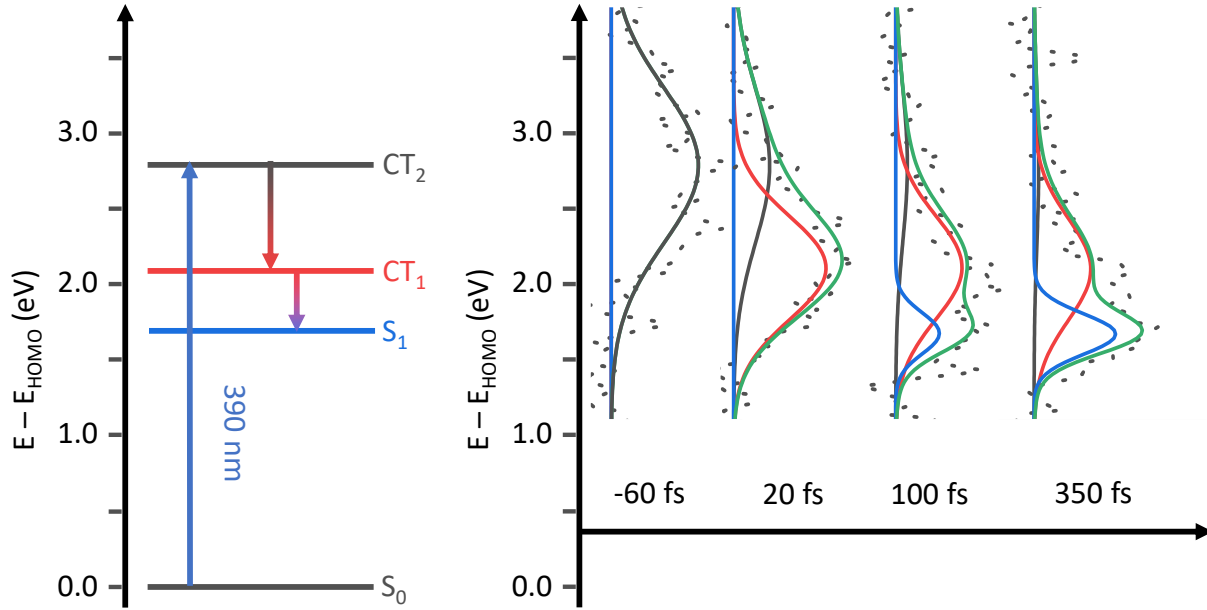


FIG. 1: *Excited state dynamics of the pristine $Sc_3N@C_{80}$ film for selected time delay steps, complementing figure 1a-c of the main text.* On the *left* side, the energy level diagram for the pristine $Sc_3N@C_{80}$ film is shown, as presented and discussed in the main text. On the *right* side, energy cuts at selected pump-probe time delays are plotted on the same energy axis as the energy level diagram on the left side, in arbitrary units (*black dots*). The overall fitting function and the individual Gaussian peaks used for the fit are included as colored lines. While position and linewidth were constrained to constant values, the peak area, representing the transient population of each excited state, is the only free parameter of the fitting routine. The resulting transient population (area) of all three Gaussian curves are plotted in figure 1c of the main text. The Gaussian curve modelling CT_2 (*solid black*) has a width of $\Delta E = 0.75$ eV and a position of $E - E_{HOMO} = 2.8$ eV, the second Gaussian, modelling CT_1 (*solid red*) has a width of $\Delta E = 0.5$ eV and a position of $E - E_{HOMO} = 2.1$ eV and the Gaussian modelling S_1 (*solid blue*) has a width of $\Delta E = 0.2$ eV and a position of $E - E_{HOMO} = 1.7$ eV.

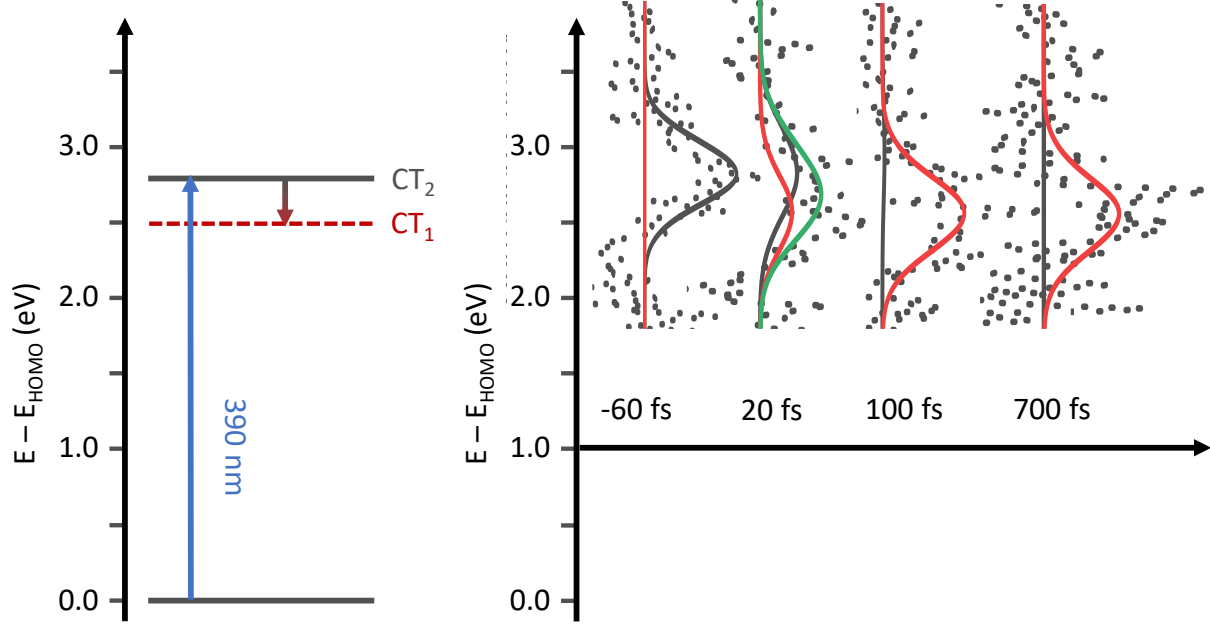


FIG. 2: *Excited state dynamics of the K intercalated $K_1(Sc_3N@C_{80})$ film for distinct time delay steps, complementing figure 2a-c of the main text.* On the *left* side, the energy level diagram for the K intercalated $K_1(Sc_3N@C_{80})$ film is shown, as presented and discussed in the main text. On the *right* side, energy cuts at selected pump-probe time delays are plotted on the same energy axis as the energy level diagram on the left side, in arbitrary units (*black dots*). The overall fitting function and the individual Gaussian peaks used for the fit are included as colored lines. While position and linewidth were constrained to constant values, the peak area, representing the transient population of each excited state, is the only free parameter of the fitting routine. The resulting transient population (area) of all three Gaussian curves are plotted in figure 2c of the main text. The Gaussian modelling CT_2 (*solid black*) has a width of $\Delta E = 0.7$ eV and a position of $E - E_{HOMO} = 2.8$ eV, the second Gaussian, modelling CT_1 (*solid red*) has a width of $\Delta E = 0.6$ eV and a position of $E - E_{HOMO} = 2.45$ eV.

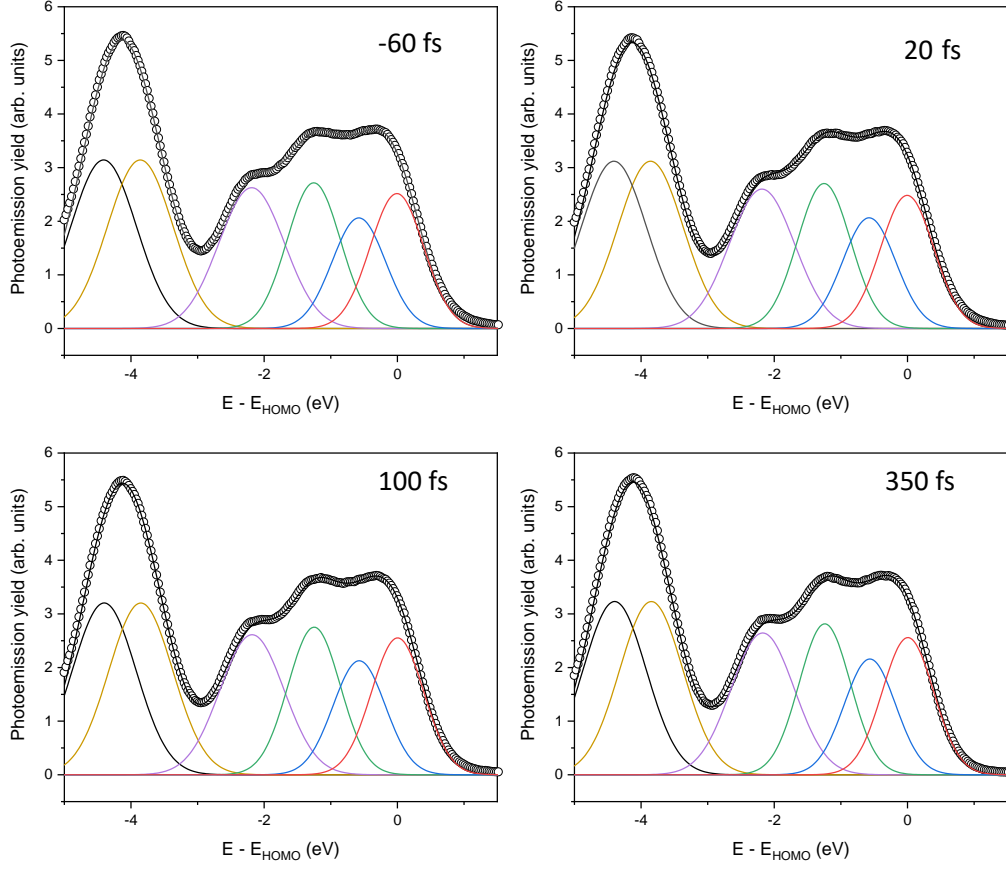


FIG. 3: *Fitting model for the transient linewidth broadening of the valence band structure at selected time delays, complementing figure 1d of the main text.* The spectra have been recorded using the snapshot mode of our detector ($E_{\text{pass}} = 100 \text{ eV}$) together with our femtosecond-XUV light source ($h\nu = 22.2 \text{ eV}$). Each datapoint is calculated from a 2D image with axis of kinetic electron energy E_{kin} versus electron emission angle Θ for a fixed pump-probe delay. Changing the pump-probe time delay Δt , we acquire our 3D-data stack $I(E_{\text{kin}}, \Theta, \Delta t)$. To obtain the shown 1D plots, we extract a cut along the energy and average the information in a small angle region of around 3° . The fitting routine is a two-step process, starting with an exponential background subtraction, which has already been performed for the data shown above. The second step consists of analyzing the spectral line-shape of the valence band, using the least number of Gaussian peaks needed for a decent description of the spectrum. After optimizing the absolute position, width and area of each Gaussian peak to match the spectral line-shape of the quasi-static spectrum at $\Delta t = -250 \text{ fs}$, the relative position, area and width of all Gaussian peaks are constrained to these values during the fitting process. The result of the fit of the time-dependent data are only three free parameters, namely one free area, position and width. The underlying assumption of this approximation is that all valence states will react similarly to the perturbation induced by absorption of UV light, as demonstrated recently in our previous work¹. While the time evolution of the area and position stay constant in time within error bars, the spectral linewidth changes over time, as shown in figure 1e of the main manuscript.

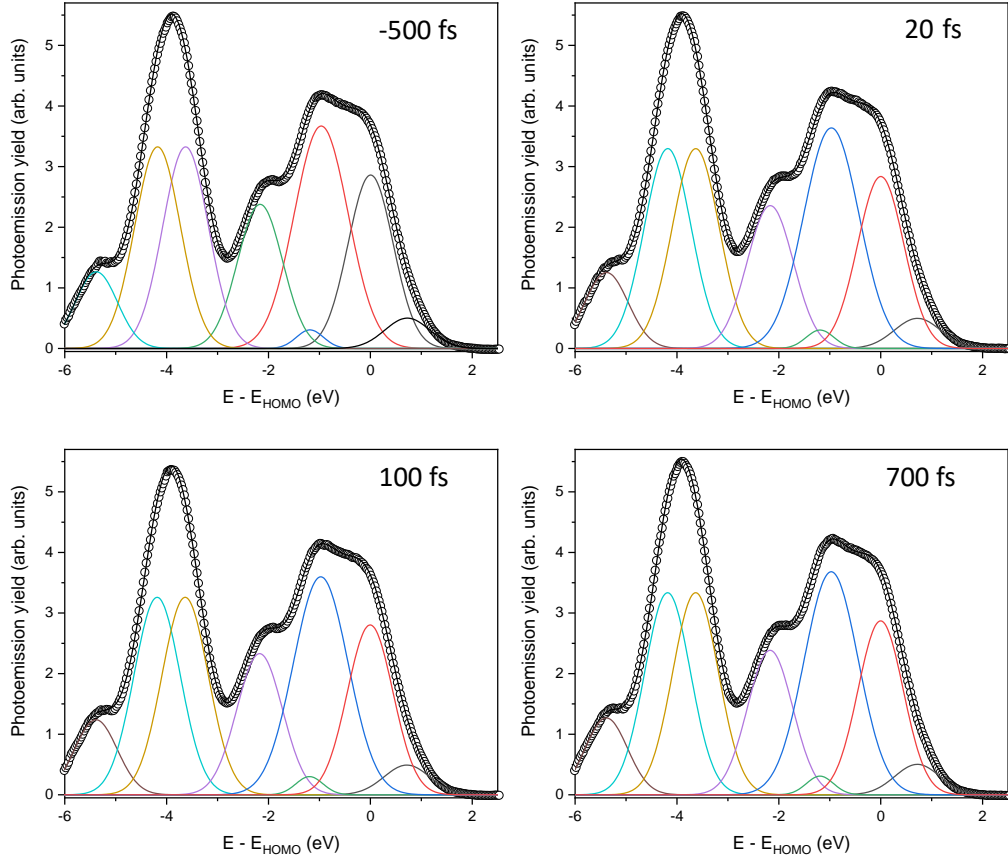


FIG. 4: Valence orbital fit of the K intercalated $K_1(\text{Sc}_3\text{N}@C_{80})$ film for distinct time delay steps, complementing figure 2d of the main text. For details about the fitting procedure for the valence band photoemission spectra shown here, see caption of figure 3 of the supplementary information.

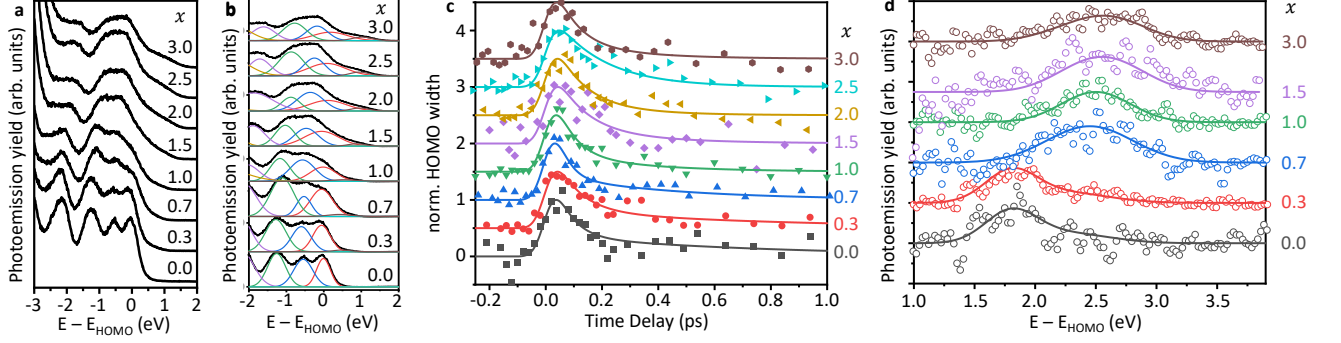


FIG. 5: Static valence band spectra, transient linewidth broadening and excited state population for different intercalation steps x of the $K_x(Sc_3N@C_{80})$ film at a time delay of 300 fs, complementing figure 3 of the main text. **a** Static valence band spectra taken for each intercalation step x , plotted in a similar way as previously by Alvarez *et al.*². The spectral shape of these valence band photoemission data sets was used to calibrate the K concentration x , the absolute intercalation density per $Sc_3N@C_{80}$ molecule. **b** UPS valence spectra with Gaussian curves used to model the valence states, as plotted in figure 3a of the main text, but for each intercalation step. **c** Normalized transient linewidth broadening of HOMO, extracted from the fs pump-probe spectroscopy valence spectra for all K concentrations x , as plotted in figure 3c of the main text. **d** Excited state spectra recorded at $\Delta t = 300$ fs for the pristine ($x = 0$) and K-intercalated film with different K concentrations x . The spectra are vertically shifted for better visibility. At $\Delta t = 300$ fs, the excited state spectra of the pristine and marginally K-intercalated film already reveal the spectroscopic signature of the Frenkel-like S_1 exciton together with the residual intensity of the CT_1 exciton on its high energy side. In contrast, the other spectra show a broad spectral feature at $E - E_{HOMO} = 2.45$ eV. This is the signature of the CT_1 exciton before exciton dissociation.

2. SUPPLEMENTARY METHODS

2.1. Experimental Setup

The $\text{Sc}_3\text{N@C}_{80}$ molecules were evaporated *in situ*, using a Knudsen cell at a temperature of 520°C, onto an Ag(111) single crystalline surface prepared by cycles of Ar^+ -sputtering and followed by annealing under UHV ($< 10^{-9}$ mbar) conditions. The $\text{Sc}_3\text{N@C}_{80}$ multilayer film was prepared in several subsequent steps. First, a multilayer has been evaporated, which then has been annealed to a monolayer film by thermal desorption. At this preparation stage, the characteristic LEED pattern of the monolayer film can be observed³. At higher scattering energies, the substrate spots of the Ag(111) crystal can be observed again. Second, we evaporated a multilayer of $\text{Sc}_3\text{N@C}_{80}$ molecules, showing no additional diffraction spots in LEED and no valence bands of the substrate in photoemission. The spectral shape of the $\text{Sc}_3\text{N@C}_{80}$ film is in very good agreement with literature^{2,3}. For the K intercalation, a Saes Getters alkali metal dispenser was used. The effective potassium (K) concentration was estimated by comparison of the valence band UPS spectra with reference spectra from literature². The time-resolved photoemission spectroscopy (trPES) measurements have been performed in a pump-probe setup with our fs-XUV light source⁴, emitting p-polarized light pulses with 20 ± 16 fs pulse duration and 22.2 eV photon energy. A time-delayed, sub-50 fs, p-polarized, 3.2 eV light pulse has been used to excite the electron system of the molecular film. This technique allows one to simultaneously observe both the dynamics of directly excited electrons (exciton dynamics) and the ensemble dynamics of the surrounding film (polaron dynamics), revealing the spectroscopic signature for the charge state of the optically excited excitons¹. For both trPES and UPS measurements, our state-of-the-art hemispherical electron analyzer Specs Phoibos 150 has been used in normal emission. Together with the chosen lens settings, this enables us to resolve a momentum regime of $k_{||} = \pm 0.5 \text{ \AA}^{-1}$ around the $\bar{\Gamma}$ -point. The molecular valence band spectra discussed in this paper are averaged over this momentum range.

2.2. Details on the spectral analysis of excited states

To extract the transient population dynamics of the different excited states from the acquired raw data, we generated energy distribution curves (EDCs) for each pump-probe time delay by integrating over the electron emission angle degree of freedom recorded by our hemispherical analyzer. Thereafter, the obtained 1D spectra were averaged over the multiple delay scans recorded within the measurement. In a next step, a Gaussian background was subtracted for every time delay of the scan. The data obtained this way is plotted in Fig. 1 and 2 of the supplementary information (SI) for distinct time steps (dotted lines). Furthermore, by application of a sliding average for the delay time and a smoothing in energy, the overview graphs in figure 1a and 2a of the main text have been created from this data. Subsequently, we analyzed the spectral shape of the excited states of the unsmoothed, background subtracted data by fitting each spectrum individually with three Gaussians. During the fitting procedure, the width and the peak positions were constrained to constant values. The peak positions and the peak width were optimized by iteratively repeating the fitting procedure with different, but time-independent width and position values. The only free fitting parameters are thus the peak heights of the three Gaussians. In Fig. 1 and 2 of the SI, the found positions and widths are plotted together with the fit curve and the raw data for distinct time delays. The delay time dependent Gaussian peak area, being the observable describing the transient population of the respective excited states is shown in figures 1c and 2c of the main text.

2.3. Details on the analysis of the population decay of the excited states

From the transient peak areas obtained by the orbital fit of the excited states presented in the previous section, population decay constants of the excited states CT_2 and CT_1 have been extracted by fitting their time dependent intensity evolution by the exponential fitting function $F_{CT_2}(t)$ and $F_{CT_1}(t)$:

$$F_{CT_2}(t) = G(t) \otimes \begin{cases} I_0 & t < t_0 \\ I_{CT_2} e^{-(t-t_0)/\tau_{CT_2}} & t \geq t_0 \end{cases} \quad (1)$$

$$F_{CT_1}(t) = G(t) \otimes \begin{cases} I_0 & t < t_0 \\ I_{CT_1} e^{-(t-t_0)/\tau_{CT_1}} (1 - e^{-(t-t_0)/\tau_{CT_1,R}}) & t \geq t_0. \end{cases} \quad (2)$$

I_0 is the background intensity, τ_{CT_2} the decay constant of the CT_2 level, $\tau_{CT_1,R}$ the rise time of the intensity of the CT_1 level, and τ_{CT_1} the decay constant of the CT_1 level. For the data analysis, the fit functions were convoluted with a normalized Gaussian function $G(t)$ with $T_{p-p} = 70$ fs. The latter value corresponds to the pump-probe cross correlation on the sample surface and was determined experimentally. The best fitting results were obtained for $\tau_{CT_1,R} = \tau_{CT_2}$. The corresponding fitting functions are shown as solid lines in figure 1c and 2c of the main manuscript. To describe the transient CT_1 population, a double-exponential decay with refilling has been assumed, similar to the method presented in the next section.

2.4. Details on the analysis of the transient width dynamics of the occupied valence band states

After having obtained the valence orbital widths as described in the caption of figure 3 of the SI, the decay constants of the fast decay channel τ_{TB_2} and the slow decay channel τ_{TB_1} can be extracted from the width ΔE using the following relation:

$$\Delta E(t) = G(t) \otimes \begin{cases} \Delta E_0 & t < t_0 \\ \Delta E_0 + \Delta E_{TB_2} e^{-(t-t_0)/\tau_{TB_2}} + \Delta E_{TB_1} e^{-(t-t_0)/\tau_{TB_1}} (1 - e^{-(t-t_0)/\tau_{CT_2}}) & t \geq t_0. \end{cases} \quad (3)$$

Here, $G(t)$ is a Gaussian function with a temporal width $T_{p-p} = 70$ fs, introduced to consider the temporal broadening introduced by the pump and probe pulse. The fit function describes a double-exponential decay process with refilling to model the two subsequent decay steps observed in the excited states. The fit functions obtained using this method are plotted in figures 1e, 2e and 3c of the main text together with the respective data.

-
- ¹ B. Stadtmüller, S. Emmerich, D. Jungkenn, N. Haag, M. Rollinger, S. Eich, M. Maniraj, M. Aeschlimann, M. Cinchetti, and S. Mathias, *Nat. Commun.* **10**, 1 (2019).
- ² L. Alvarez, T. Pichler, T. Pichler, P. Georgi, T. Schwieger, H. Peisert, L. Dunsch, Z. Hu, M. Knupfer, J. Fink, et al., *Phys. Rev. B* **66**, 351071 (2002).
- ³ J. Seidel, L. L. Kelly, M. Franke, G. Van Straaten, C. Kumpf, M. Cinchetti, M. Aeschlimann, and B. Stadtmüller, *Phys. Rev. B* **98**, 1 (2018).
- ⁴ S. Eich, A. Stange, A. Carr, J. Urbancic, T. Popmintchev, M. Wiesenmayer, K. Jansen, A. Ruffing, S. Jakobs, T. Rohwer, et al., *J. Electron Spectros.* **195**, 231 (2014).